

Synthesizing degree of polarization uniformity from non-polarization-sensitive optical coherence tomography signals by neural network

SHUICHI MAKITA,^{1*} MASAHIRO MIURA,² SHINNOSUKE AZUMA,³
TOSHIHIRO MINO,³ AND YOSHIAKI YASUNO¹

¹Computational Optics Group, University of Tsukuba, 1-1-1 Tennodai, Tsukuba, Ibaraki 305-8573, Japan

²Department of Ophthalmology, Tokyo Medical University Ibaraki Medical Center, 3-20-1 Chuo, Ami, Ibaraki 300-0395, Japan

³Topcon Corporation, 75-1 Hasunumacho, Itabashi, Tokyo 174-8580, Japan

*shuichi.makita@cog-labs.org

<http://optics.bk.tsukuba.ac.jp/COG/>

Abstract: The degree of polarization uniformity (DOPU) imaging by polarization-sensitive optical coherence tomography (PS-OCT) has the potential to provide biomarkers in retinal diseases. It highlights abnormalities in the retinal pigment epithelium that is sometimes not clear in the OCT intensity images. However, the PS-OCT system is rather complicated than conventional OCT. We present a neural-network-based approach to estimate the DOPU from standard OCT images. A neural network was trained to synthesize DOPU from single-polarization-component OCT intensity images by targeting DOPU images. Synthesized DOPU images were generated by the neural network, and the clinical findings from ground truth DOPU and synthesized DOPU were investigated. There is a good agreement in the findings of the RPE abnormalities; 0.869 of recall and 0.920 of precision among 20 cases with retinal diseases. In 5 cases of healthy volunteers, no abnormalities were found in synthesized DOPU as well as ground truth DOPU. The proposed neural-network-based DOPU synthesizing method shows the potential to extend the features of retinal non-PS OCT.

© 2022 Optica Publishing Group under the terms of the [Optica Open Access Publishing Agreement](#)

1. Introduction

Optical coherence tomography (OCT) [1] visualizes cross-sectional images of the posterior eyes non-invasively and provides morphological structures of retinal layers. OCT is used for diagnosis and follow-up retinal treatment [2]. Recently, degree-of-polarization uniformity (DOPU) imaging [3–5] by polarization-sensitive (PS-) OCT has been applied to investigate abnormalities of the retinal pigment epithelium (RPE) [6–20]. These show that DOPU imaging and DOPU analysis can be utilized for the detection and investigation of RPE anomalies. Hence, DOPU is a potential biomarker of RPE abnormalities.

Although DOPU has a lot of potential in retinal diagnosis, its widespread use is prevented by the extra cost of PS-OCT setup. DOPU is a randomness metric of the polarization state of the backscattered probe beam. To detect the polarization state of the backscattered probe light, at least two detectors and polarization splitter and controller are required, while a standard OCT generally requires only one detector. If DOPU can be obtained from the conventional OCT with the single polarization component detection, this will extend the applications of the existing OCT devices.

Scattering of light by dense scatterers (multiple scattering) [21, 22] and anisotropic scatterers [23] have been considered as possible causes of polarization randomization, and these scattering properties may affect the formation of speckles in OCT intensity images [24, 25].

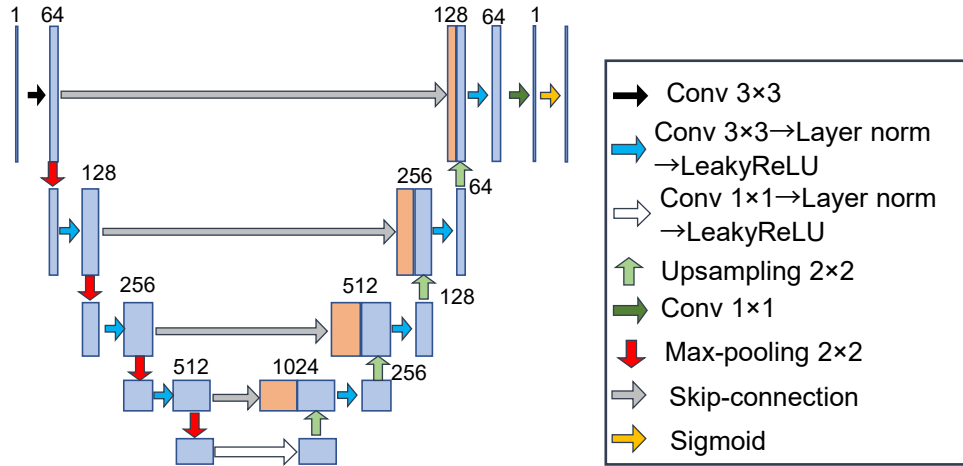


Fig. 1. The neural network architecture for synthesizing DOPU.

However, it is not straightforward to relate between them, and solving this is difficult. The deep neural network is used to find a practical solution to an inverse problem [26] and also can be used to restore hidden structure by speckles [27] and infer scattering properties [28]. We hypothesize that the deep neural network technique can find features related to polarization randomization in speckles and synthesize the appearances of the RPE, as in DOPU.

In this paper, we proposed the neural-network-based approach to synthesize DOPU from standard OCT signals to get over the difficulties. A neural network was trained with the pairs of OCT intensity and corresponding DOPU images. The trained network synthesized DOPU images from unseen OCT intensity images. The network's performance was evaluated by a grader by counting the clinical findings from each DOPU image.

2. Methods

We collect data using a prototype OCT device (Section 2.2). Both of DOPU and OCT intensity are generated (Section 2.3), and used to train (Section 2.4 and 2.5) and evaluate (Section 2.6) a neural network for synthesizing DOPU images (Section 2.1). The details of each step are following.

2.1. Architecture of *syn-DOPU* network

The network used in this study is based on the U-Net [29], and its architecture is presented in Fig. 1. The input OCT intensity image first passes a 3×3 convolution layer and increases channels to 64. In the encoder, the sequence of 3×3 convolution, layer normalization [30], and Leaky ReLU activation function [31] (slope for negative values = 0.01) is applied followed by 2×2 maxpooling. The input image size is halved by the operation, while the number of channels is doubled. This successive operation is applied four times in total. In the decoder, 2×2 upsampling is applied to reconstruct the output from extracted features. Then, the image is concatenated with corresponding images coming from the encoder part via a skip-connection path. The sequence of 3×3 convolution, layer normalization, and Leaky ReLU activation is applied, while the number of channels is reduced by a quarter. A 1×1 convolution is applied to reduce the number of channels from 32 to 1 to output an image. Finally, a customized sigmoid function is applied to optimize the network's output within the range from 0 to 1, which is the realizable DOPU value.

2.2. Data collection

A clinical polarization diversity (PD)-OCT was used in this study [32]. This system does not have precise control of the polarization state of the probe beam, and only a compact polarization-diversity receiver (PDR) is installed to a standard swept-source OCT. Different from a standard PS-OCT, this system cannot measure phase retardation but only DOPU with the minimum setup.

Briefly, the light source is a wavelength sweeping laser (1 μm with a sweep rate of 100 kHz). The backscattered light is combined with the reference light, and finally, two orthogonal polarization components of the backscattered light are acquired by two detection channels of the PDR. The sensitivity with each channel is 89.5dB. The axial resolution is 6 μm in tissues defined by full-width at half maximum, and the lateral resolution is 20 μm expected from $1/e^2$ beam spot diameter.

Human eyes have been scanned with the raster scan protocols (6 mm with 512 A-lines and 3 mm with 300 A-lines). Four repeated B-scans are obtained at the same location. Thirty-one volunteers without ophthalmic abnormalities (43 eyes) and 351 patients (478 eyes) have been scanned. The study was approved by the Institutional Review Boards of Tokyo Medical University and adhered to the tenets of the Declaration of Helsinki. The nature of the present study and the implications of participating in this research project were explained to all study participants, and written informed consent was obtained from each participant before any study procedures or examinations were performed.

2.3. Signal processing

DOPU and OCT intensity were computed from the two OCT signals of orthogonal polarization components of the backscattered probe beam. A modified DOPU reconstruction algorithm with computing Stokes vectors [5] was used for the computation.

At first, the noise-bias-corrected Stokes vector is computed as follows,

$$\begin{bmatrix} s'_0(x, z, f) \\ s'_1(x, z, f) \\ s'_2(x, z, f) \\ s'_3(x, z, f) \end{bmatrix} = \begin{bmatrix} |g_H(x, z, f)|^2 + |g_V(x, z, f)|^2 - [n_H(z) + n_V(z)] \\ |g_H(x, z, f)|^2 - |g_V(x, z, f)|^2 - [n_H(z) - n_V(z)] \\ 2\text{Re}[g_H(x, z, f)g_V^*(x, z, f)] \\ 2\text{Im}[g_H(x, z, f)g_V^*(x, z, f)] \end{bmatrix}, \quad (1)$$

where $g_H(x, z, f)$ and $g_V(x, z, f)$ are complex OCT signals obtained from the H - and V -polarization channels, x, z denote the lateral and axial axes, f denotes the frame number along taken at the same position, Re and Im are operators to take only real or imaginary value, respectively, and $n_H(z)$ and $n_V(z)$ are the standard deviation of background data in each channel. From the stokes vector [Eq. 1], DOPU is calculated from N frames as follows,

$$\text{DOPU}(x, z) = \frac{\sum_{f=1}^N \sqrt{\frac{3}{\sum_{m=1}^3 \overline{s'_m{}^2}(x, z, f)}}}{\sum_{f=1}^N \overline{s'_0}(x, z, f)}, \quad (2)$$

where $\overline{s'_m}$ is the spatially averaged m -th stokes parameter. In this study, moving averaging with 3×3 pixels is used.

Corresponding OCT intensity is obtained from the coherent composition of each channel and complex-averaging of repeated scans [33], and then the absolute values are calculated as follows,

$$I(x, z) = \left| \frac{1}{N} \sum_{f=1}^N e^{-i\Delta\phi_f(x, z, f)} \left[g_H(x, z, f) + e^{-i\Delta\phi_{ch}(x, f)} g_V(x, z, f) \right] \right|^2, \quad (3)$$

where $\Delta\phi_f$ and $\Delta\phi_{ch}$ are the mean phase difference between frames and channels, respectively. This can be thought of as mimicking the complex fields of the probe and the reference beams before splitting them into two orthogonal polarization components with the PDR and taking the OCT signal composed of them. This OCT signal corresponds to the elliptically polarized single polarization component whose long axis is aligned with the polarizer in the PDR of the backscattered probe beam. The complex averaging of repeated frames corresponds to a longer integration time. Hence, this OCT intensity image is essentially the conventional single-detector OCT image.

2.3.1. Pre-processing for neural network

DOPU is defined within the range of [0, 1], and the network (Section 2.1) output is within this range. However, the DOPU [Eq. 2] with the noise-bias-corrected Stokes vectors [Eq. 1] exceeds the range of [0, 1] at low signal-to-noise ratio (SNR) regions because of the stochastic nature of noises. The following process was applied to the DOPU images to treat invalid DOPU values as [5]:

$$\text{DOPU}'(x, z) = \begin{cases} \text{DOPU}(x, z) & 0 < \text{DOPU}(x, z) < 1 \\ 1 & \text{otherwise} \end{cases}. \quad (4)$$

For supplying to NN, OCT intensity is converted into SNR.

$$I'(x, z) = (I(x, z) - \mu) / \sigma, \quad (5)$$

where μ is the background offset and σ is the standard deviation of the background.

2.4. Dataset for training

Twenty-six healthy volunteers (38 normal eyes) and 330 patients (457 pathological eyes) were included in the training & validation datasets. The pathological cases include 145 age-related macular degeneration (AMD), 42 central serous chorioretinopathy (CSR), 22 Vogt-Koyanagi-Harada disease (VKH), 17 retinal vein occlusion, 13 diabetic macular edema, 13 myopia, and others. Three pairs of OCT intensity and DOPU B-scans were extracted from each volume. Then, multiple 64×64-pixel patches, where the area less than 5-dB SNR is smaller than 85%, were extracted from each B-scan.

2.5. Training process

The schematic diagram of the network training is shown in Fig. 2. The dataset was divided 8:2 by subject into training and validation. The total number of patches used for training is 69,478 (284 subjects), and 17,382 patches (72 subjects) are used for validation.

To increase the variety of training data, the following data augmentations have been applied during the network training: horizontal flipping, resizing, SNR penalizing, offset adding, and scaling. As shown in Fig.2, spatial data augmentation were applied for both input OCT intensity and target DOPU images. Both are randomly flipped in the horizontal direction and resized with magnifications of [1, 2] in the axial and [1, 4] in the horizontal directions, respectively. Data augmentations for OCT intensity values follow. Random SNR penalizing from 0 to -15 dB, scaling from 0.01 to 100 times, and offset adding from 0 to 1,000 are applied. The details of the SNR penalizing are in Appendix A.

Binary cross entropy between the output of the network and the corresponding target DOPU is used as the loss function.

$$L_{\text{BCE}} = \sum_{n,w,h} - [y_{n,w,h} \log(x_{n,w,h}) + (1 - y_{n,w,h}) \log(1 - x_{n,w,h})], \quad (6)$$

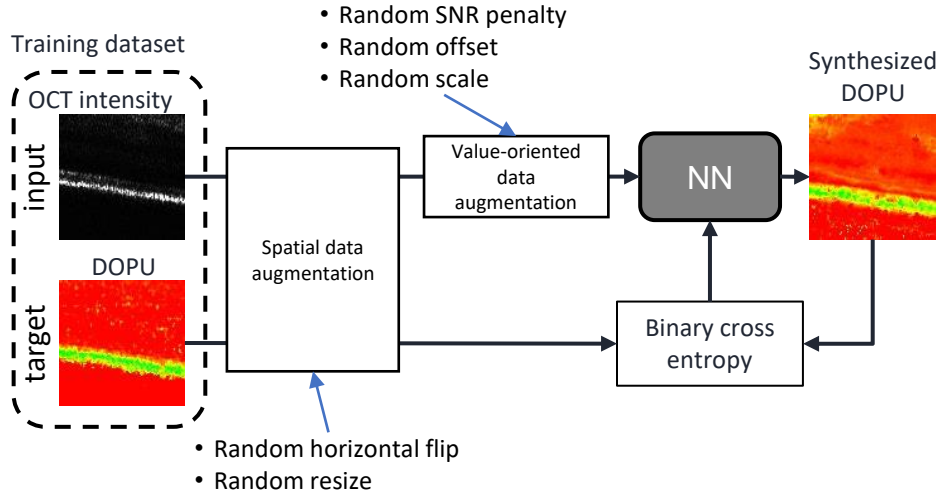


Fig. 2. Outline of the training. A set of OCT intensity and DOPU in the dataset are randomly flipped in the horizontal direction and resized. For OCT intensity value, random SNR penalizing, offset adding, and scaling are randomly applied and input to the NN. A loss value is obtained between the output of the NN and the target DOPU using binary cross entropy.

where x is the output of the NN, y : the target DOPU, n, w, h are indices of a pixel in a minibatch with a batch size of N , image width of W , and image height of H . The NN was trained with minibatch learning with a batch size of 64. Adam optimizer [34] with a learning rate of 0.001 and momentum parameters $\beta_1 = 0.9$, $\beta_2 = 0.999$ was used. The training was stopped when the validation loss did not improve in the last 20 epochs. And the epoch that exhibits the minimum validation loss is used as the trained network.

2.6. Evaluation of DOPU synthesizing

We evaluated the trained DOPU synthesizing network from the perspective of clinical utility. In the evaluation, 5 volunteers (5 normal eyes) and 20 patients (20 pathological eyes) are included, which are not included in the training & validation datasets. The pathological eyes include 12 AMD, 5 CSR, 2 pachychoroid, and 1 myopia. The DOPU and synthesized DOPU (syn-DOPU) images of the evaluation dataset were evaluated by an ophthalmologist. Diagnostic agreements between DOPU and syn-DOPU were calculated for normal and pathological eyes. The protocols are the followings.

2.6.1. Normal eye evaluation

In each eye, 5 B-scans equally spaced along the slow scan direction were extracted. Then, the grader evaluated the DOPU and syn-DOPU to check whether there were abnormal appearances in the retina or not. Finally, the agreement of each diagnosis was evaluated.

2.6.2. Pathological eye evaluation

Another ophthalmologist looked into the OCT intensity volume data and selected the pathological region of abnormality along the slow scanning direction for each volume. Then, 5 B-scans were randomly selected from each region. And then, another ophthalmologist surveyed the DOPU and

syn-DOPU images by demarcating four types of abnormalities: RPE defect, RPE thickening, RPE elevation, and hyperreflective foci (HRF).

The relation between DOPU and syn-DOPU is classified into three types, both DOPU and syn-DOPU show an abnormality (true positive), DOPU shows an abnormality, while syn-DOPU does not show it (false negative), and DOPU does not show any abnormality, while syn-DOPU shows it (false positive). Note that the case that both DOPU and syn-DOPUs are negative (true negative) was not counted because normal regions cannot be counted in this protocol. The number of clinical findings in each DOPU was counted for each abnormality among every B-scan, and recall and precision were calculated.

3. Results

3.1. Normal eye

Figure 3 shows OCT intensity, DOPU, and syn-DOPU of all 5 normal cases in the evaluation dataset. In all eyes, the whole appearance of DOPU is well reproduced in syn-DOPU. There are no abnormal appearances found in all 25 syn-DOPU images, as same as the DOPU images. Sometimes, the DOPU images exhibit a low DOPU value at the inner limiting membrane of the fovea (white arrow in Fig. 3). This appearance is not reproduced in the corresponding syn-DOPU image. The syn-DOPU images well generated a normal distribution of DOPU.

3.2. Pathologic cases

Figure 4 shows the OCT intensity, DOPU, and syn-DOPU images of 5 pathological cases. AMD #1 exhibits the detachment of the hyper-scattering layer in the OCT intensity image [orange arrow, Fig. 4(a)] where DOPU values are high in both DOPU and syn-DOPU [Figs. 4(b) and 4(c)]. Both DOPU and syn-DOPU images are graded to have RPE defects at the retina-choroid boundary (black arrows), where apparent abnormalities are not observed in the OCT intensity image. In AMD #2, there is the detachment of hyper-scattering layer in OCT intensity image as same as AMD #1 (orange arrow), which is graded as RPE elevation in both DOPU and syn-DOPU. In addition, the thickening of the hyper-scattering layer appeared in OCT intensity image, and it is graded as the RPE thickening in both DOPU and syn-DOPU images (white arrow). The RPE seems to be elevated in both AMD #1 and #2 in OCT intensity images (orange arrows). However, the DOPU image of AMD #1 [Fig. 4(b)] does not show low DOPU signals, while that of AMD #2 [Fig. 4(e)] shows low DOPU signals (graded as the RPE elevation, orange arrows). This tendency is correctly reproduced in the syn-DOPU images [Figs. 4(c) and 4(f)]. This indicates the possibility of the proposed method to generate biomarkers of RPE abnormalities obtained by DOPU without PS-OCT setup.

In AMD #3, HRF is shown in both DOPU and syn-DOPU images [blue arrows, Figs. 4(h) and 4(i)]. However, some HRFs do not appear in syn-DOPU. Meanwhile, some cases exhibit abnormalities in syn-DOPU, which are not observed in DOPU. In AMD #4, RPE elevation is observed by the grader in DOPU [white arrow, Fig. 4(k)]. The RPE defect is observed in syn-DOPU [black arrow, Fig. 4(l)], which is not observed in DOPU.

The findings of the RPE abnormalities in DOPU and syn-DOPUs are summarized in Table. 1 The recall of each abnormality was 0.889 (RPE defect), 0.88 (RPE thickening), 1 (RPE elevation), and 0.429 (HRF). The precision of each abnormality was 0.744 (RPE defect), 1 (RPE thickening), 1 (RPE elevation), and 1 (HRF). The recall and precision of all four abnormalities are 0.869 and 0.920, respectively. Overall, the findings of RPE abnormalities are well generated by syn-DOPU.

In addition, a VKH case is also evaluated. As progress the VKH, choroidal melanin is reduced [35], and the choroidal DOPU values increased [36,37] The syn-DOPU image of the VKH case [Fig. 4(o)] shows the high DOPU value at the choroid as same as the DOPU [Fig. 4(n)]. Syn-DOPU will also be available to generate biomarkers of choroidal pigmentation, not only for

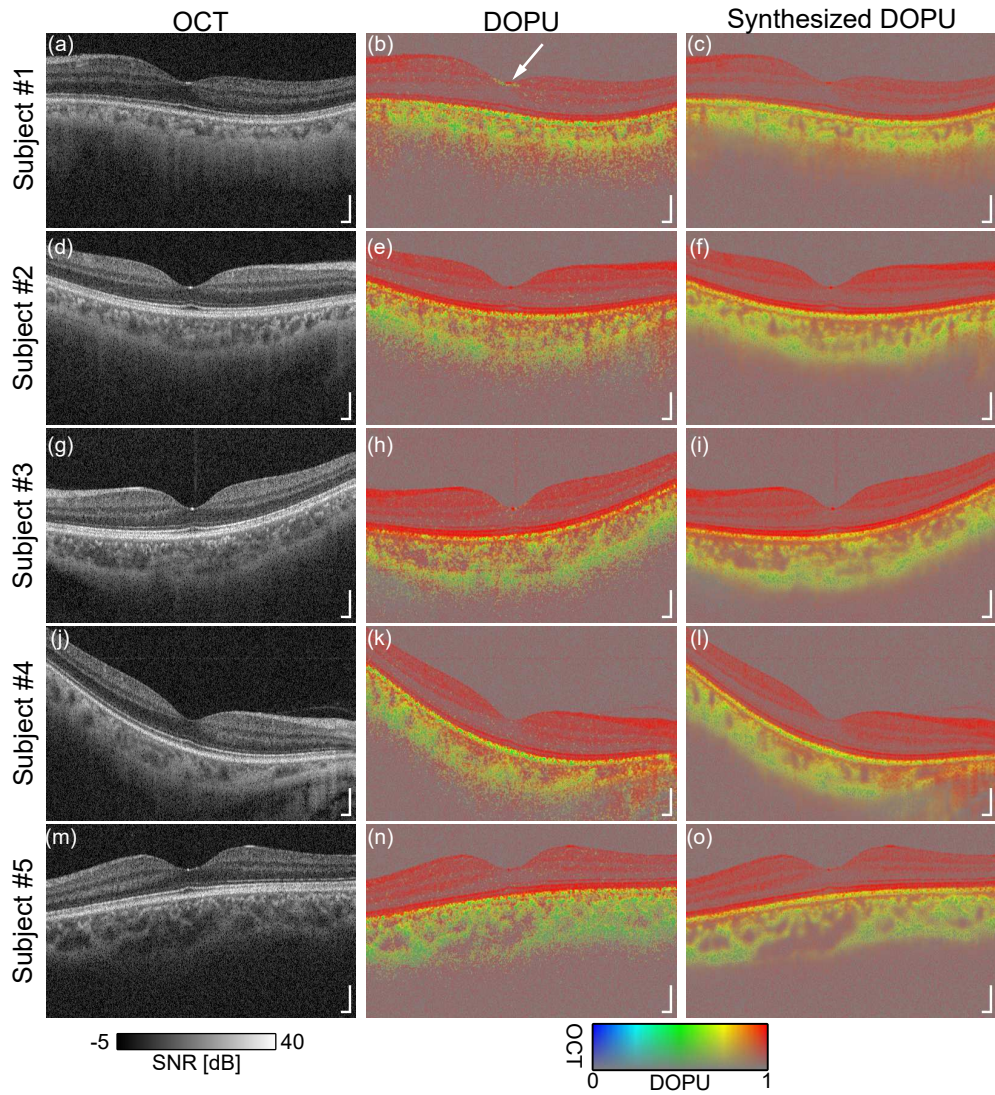


Fig. 3. Inference of synthesized DOPU for 5 eyes of 5 normal subjects. (a, d, g, j, m) OCT, (b, e, h, k, n) DOPU, and (c, f, i, l, o) synthesized DOPU cross-sectional images. Scale bars indicate 200 μ m.

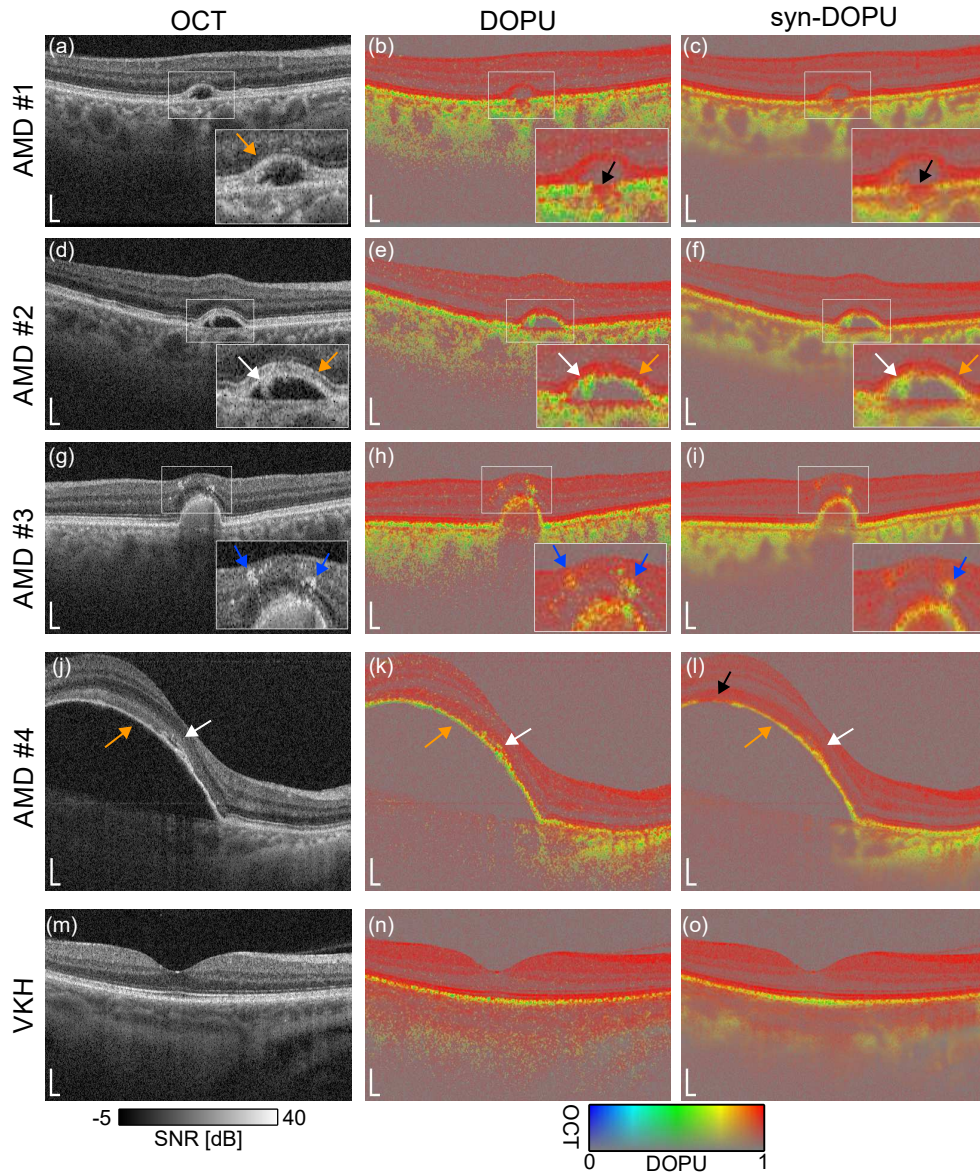


Fig. 4. Inference of synthesized DOPU for 5 eyes of 5 pathological cases. (a, d, g, j, m) OCT intensity, (b, e, h, k, n) DOPU, and (c, f, i, l, o) synthesized DOPU cross-sectional images. Four types of RPE abnormalities are indicated by arrows, i.e., the RPE defects (black), RPE elevation (orange), RPE thickening (white), and HRF (blue). In VKH, both DOPU and synthesized DOPU exhibit high DOPU values in the choroid. Scale bars indicate 200 μm.

Table 1. The summary of clinical findings observed from DOPU and syn-DOPU independently. RPE defect, RPE thickening, RPE elevation, and HRF were analyzed by an ophthalmologist.

	# of findings			Recall	Precision
	DOPU (+) Syn-DOPU (+)	DOPU (+) Syn-DOPU (-)	DOPU (-) Syn-DOPU (+)		
RPE defect	32	4	11	0.889	0.744
RPE thickening	22	3	0	0.88	1
RPE elevation	63	0	0	1	1
HRF	9	12	0	0.429	1
Total	126	19	11	0.869	0.920

the RPE abnormalities.

4. Discussion

4.1. Signal source of syn-DOPU

The proposed network was trained to synthesize DOPU from OCT intensity images corresponding to one polarization component, although the real DOPU is calculated from two polarization components obtained by PS-OCT. There is a lack of polarization information in input for the network. Hence, the factors, which are used for generating features in DOPU, probably influence the OCT intensity, too.

One of them will be scattering properties [21–23]. The source of DOPU contrast in retinal imaging is considered as the melanin [3, 4]. Although the effect of polarization scrambling is only measured by a PS-OCT, different scattering properties affect the OCT intensity images by speckle formation [24, 25]. The neural network might synthesize DOPU images from features in OCT intensity images.

Another factor might be morphological patterns that appeared in OCT intensity images. Some parts of the spatial pattern are quite similar in both OCT intensity and DOPU images, such as the RPE and choroid. The U-Net might utilize the similarity of spatial structures for synthesizing DOPU images.

4.2. Interpretation of results

Normal and pathological eyes were used for the evaluation of the syn-DOPU network. The normal eye evaluation was conducted to check whether the non-abnormal region was correctly reproduced as non-abnormal in syn-DOPU images, while the pathological evaluation was conducted to check whether the NN can correctly reproduce each abnormality without missing the abnormality, confusing the other abnormalities, or synthesizing false ones.

In normal eye cases, there were no abnormalities in the 25 syn-DOPU (5 eyes) evaluation images. The proposed method faithfully synthesizes normal appearances. In the pathological eye cases, recall and precision were computed for each abnormality. The recall reveals how much this method misses abnormalities to be synthesized, while the precision reveals how many false abnormalities were synthesized which do not appear in DOPU images. The overall recall and precision of the RPE abnormalities are high (>0.85).

The precision for RPE defect is low (0.744) compared to other abnormalities (1.0). When some hyper-scattering materials surrounding the RPE as shown in AMD #4 in Fig. 4, false RPE

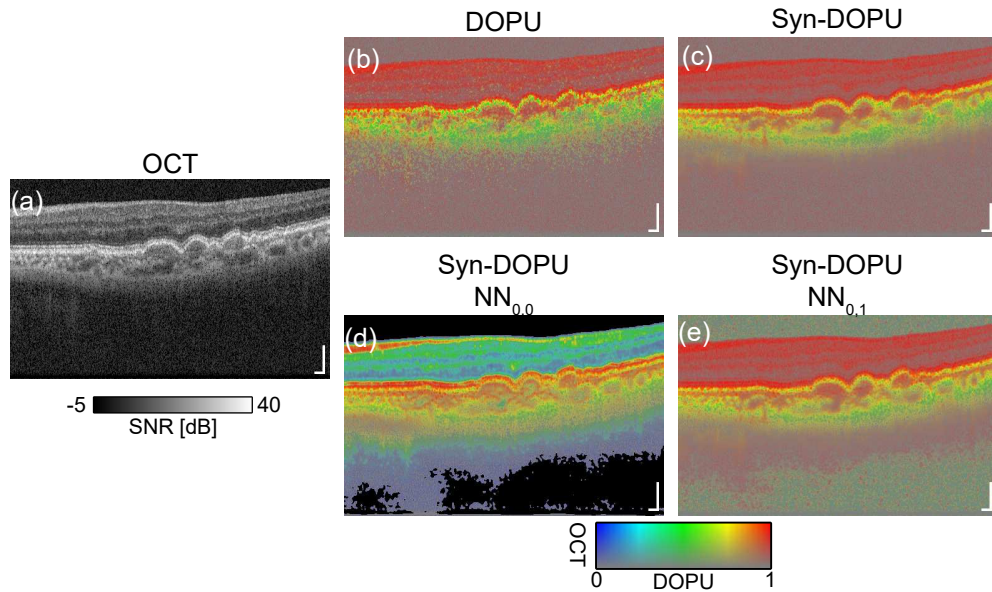


Fig. 5. Synthesized DOPU generated by the networks trained with different pre-processing for the target DOPU. (a) OCT, (b) DOPU, and (c-e) synthesized DOPU images of a subject in the evaluation dataset. Three synthesized DOPU images, (c), (d), and (e), are obtained from three networks trained with different pre-processing for target DOPU, Eqs. (4), (7), and (8), respectively. Scale bars indicate 200 μm .

defect appears. Because the U-Net uses the spatial structure, the decreased contrast between the RPE and the surrounding tissue might be a source of false defects.

The recall was especially low for HRF (0.429). Some HRFs are not well generated by syn-DOPU. This is perhaps due to the small size of HRFs. In both training and validation datasets, the occupation of the HRF region might be very small. Increasing the HRF cases in training data and weighting the abnormal regions in training will improve the synthesizing of the HRF.

4.3. Treatment of noise value in DOPU

If there is no reflection from the measurement sample, DOPU is not correctly reconstructed. In the case of the human eye, the signal deeper than the choroid cannot be well measured. After applying the depth-dependent noise correction [5], the signal will appear as noise that takes a larger value than 1 or a smaller value than 0. To ignore the noise during the training, the pre-processing in Eq. 4 was applied. In this section, the utility of the pre-processing is evaluated.

In comparison, two other pre-processing were defined,

$$M_{0,0}[x] = \begin{cases} x & 0 < x < 1 \\ 0 & \text{otherwise} \end{cases}, \quad (7)$$

and

$$M_{0,1}[x] = \begin{cases} x & 0 < x < 1 \\ 1 & x \geq 1 \\ 0 & x \leq 0 \end{cases}. \quad (8)$$

Then, the performance of pre-processing of Eqs. (4), (7), and (8) were compared. The NN were additionally trained with the pre-processing of Eqs. (7), and (8): so called as $NN_{0,0}$, and $NN_{0,1}$, respectively.

The syn-DOPU images obtained with the three networks are shown in Fig. 5. The subject in the evaluation dataset is used. In the case of $NN_{0,0}$ [Fig. 5(d)], DOPU values in the retina are erroneously low. This may be because the network is trained to generate low DOPU values in the lower SNR regions. In the case of $NN_{0,1}$ [Fig. 5(e)], DOPU values in the tissue regions are reasonable. In the noise regions, the DOPU values are around 0.5; this is the expected DOPU value, the middle of [0, 1].

The root-mean-square error (RMSE) between DOPU and syn-DOPU at low SNR regions (between 1 and 5 dB) is calculated with the evaluation dataset (25 volumes of 20 pathological and 5 healthy eyes). With the pre-processing of Eq. (4), RMSE is 0.044 ± 0.004 (mean \pm STD over 25 volumes), while $NN_{0,0}$ and $NN_{0,1}$ exhibit RMSE of 0.926 ± 0.008 and 0.269 ± 0.014 . Although syn-DOPU image obtained from the $NN_{0,1}$ [Fig. 5(e)] seems good, syn-DOPU values at the low SNR pixels are slightly departed from DOPU values. From these perspectives, we decided to use the pre-processing of Eq. (4).

4.4. Variable input image size

In the case of image generation, neural networks frequently use instance normalization [38]. However, instance normalization is not suitable for the proposed method, where the input image size is variable. We used layer normalization instead since it does not depend on the data size [30].

Figure 6 shows the synthesized DOPU images when different input image sizes are supplied. For comparison, a network with the same architecture as in Fig. 1 was trained on the same training data set (Section 2.4), except that the layer normalization layers were replaced by instance normalization layers. In the case of the network with instance normalization, DOPU is well synthesized when the input size [64 \times 64 pixels, Fig. 6(e)] is the same as that of the training dataset as shown in Fig. 6(g). However, when the input size [512 \times 640 pixels, Fig. 6(a)] is far from that of the training dataset, the synthesized DOPU [Fig. 6(c)] exhibits discrepancies in DOPU values and structure of the low DOPU regions from the ground truth DOPU image [Fig. 6(d)]. In contrast, synthesized DOPU for both input image size cases are similar and close to the ground truth with the network used in the current study [Figs. 6(b) and 6(f)]. RMSE between the DOPU and syn-DOPU with the input size of 512 \times 640 pixels is calculated with the evaluation dataset (25 volumes of 20 pathological and 5 healthy eyes). RMSE at high SNR regions (more than 1 dB) is 0.063 ± 0.005 (mean \pm STD over 25 volumes) and 0.137 ± 0.012 with the NN used in the current study (with layer normalization) and with instance normalization, respectively. The NN with layer normalization shows better inference accuracy.

4.5. Transferring to non-PS-OCT setup

In practice, the proposed method will be transferred to non-PS OCT system. Different imaging properties between the two systems will be hurdled of the application. Figure 7 shows an example normal case of syn-DOPU from a non-PS, commercial OCT device (DRI-OCT, Topcon). The spatial sampling properties of the image with the commercial OCT device are 11.7 μm / A-line and 2.6 μm / pixel. The B-scan is not averaged, hence, the SNR is lower than that of used in the training (4 B-scans are averaged in complex, Section 2.3). The syn-DOPU [Fig. 7(d)] exhibits good appearance as well as DOPU obtained by PD-OCT [Fig. 7(b)], high DOPU values in the retina and low DOPU values at the RPE and choroid. The network training with value-oriented data augmentation (Section 2.5) might be essential to accept OCT intensity images from different setups. In this study, we introduced the SNR penalizing, which is a model-based additive random noise emulation in OCT intensity images (Appendix A), as one of data augmentations. The effect of the SNR augmentation is shown by comparing to syn-DOPU without SNR augmentation

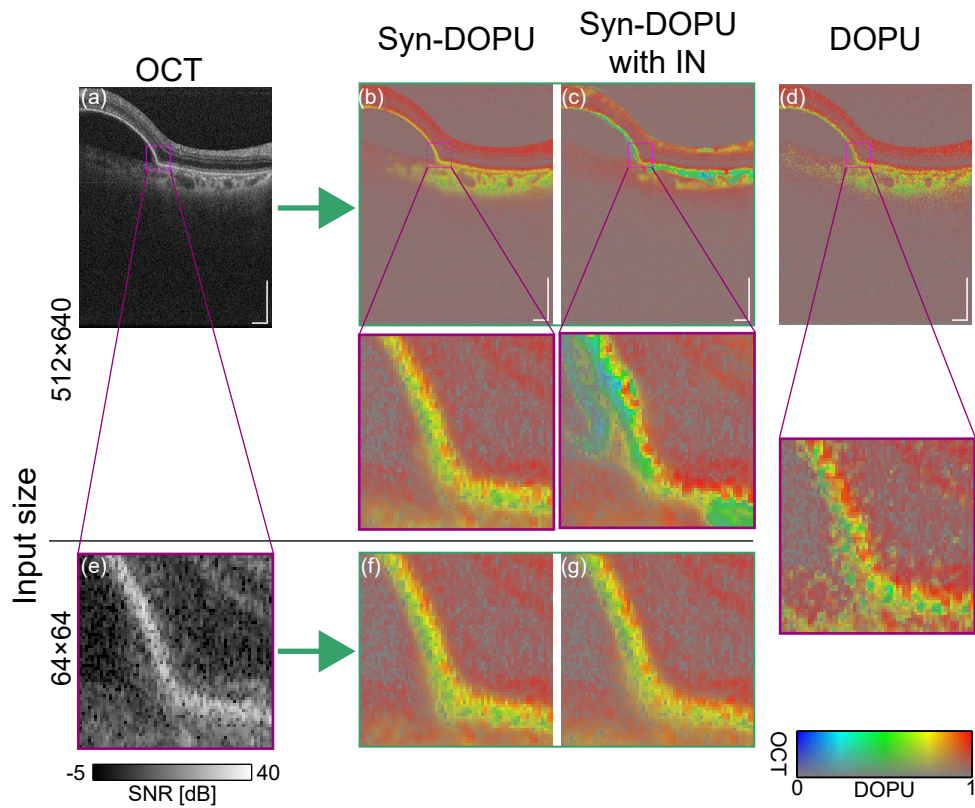


Fig. 6. Comparison of synthesized DOPU by the neural network using layer normalization and instance normalization. When the input OCT intensity size is 512x640 pixels (a), the synthesized DOPU with the network used in this study (b) is well agreed with ground truth DOPU (d). However, the synthesized DOPU generated from a network with instance normalization (c) is not well agreed with (d). If the input is cropped to the size as the same to the training dataset (512x640 pixels, e), synthesized DOPU obtained by both networks (f, g) well agreed with the ground truth. Scale bars indicate 500 μm.

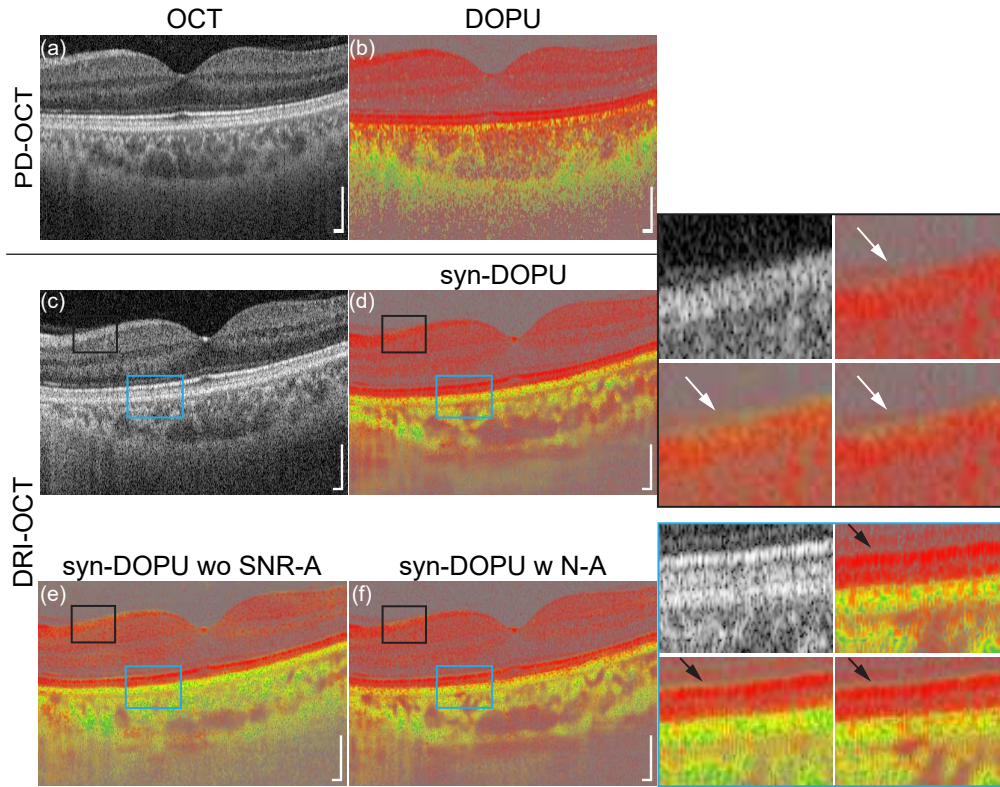


Fig. 7. Synthesized DOPU is obtained with non-PS-OCT setup. The same healthy eye has been scanned with PD-OCT (a) and a commercial OCT device (c). The synthesized DOPU obtained from the commercial OCT (d) shows no abnormalities as the same to the ground truth DOPU (b) obtained by PD-OCT. Synthesized DOPU obtained by networks trained (e) without random SNR penalizing and (f) with random exponential noises exhibits erroneous low DOPU values at the retinal nerve fiber layer (white arrows) and photoreceptor layer (black arrows). Scale bars indicate 200 μm .

[Fig. 7(e)] and with noise augmentation [Fig. 7(f)]. The case of the noise augmentation is only adding random variable to OCT intensity which obeys exponential distribution, i.e., Eq. 10 without the cross term between signal and noise. Except the case with SNR augmentation, syn-DOPU images exhibit erroneously low DOPU values at the boundary between the vitreous and the retina (white arrows) and at the inner/outer segment junction (black arrows). The proper data augmentations are required to generalize the method.

4.6. Related work of synthesizing DOPU

Synthesizing PS-OCT images from a standard OCT has also been demonstrated by Sun *et al.* [39]. They trained pix2pix GAN [40] with PS-OCT dataset and synthesized PS-OCT images, including DOPU and phase retardation, from OCT intensity images. The differences to the current studies are the sample and evaluation method.

Sun *et al.* [39] used human breast tissues, chicken skin tissue and chicken muscle tissue as the sample. Since these tissues are not melanin-rich, the tissue properties generating DOPU are probably different from the case of the retina. In these samples, the randomization of polarization state due to multiple scattering might be altered by interacting with birefringent tissues [41], and

the polarization state may be further randomized by randomly-oriented birefringent tissues [42], i.e., collagen and muscle. This also affects the OCT intensity image, and hence provides features maybe used to synthesize DOPU.

The similarity of synthesized and real images and the image-wise classification of human breast tissues are evaluated in Ref. [39]. In this study, we evaluated the synthesized DOPU images based on the potential clinical biomarkers of the RPE abnormalities. This is more directly related to the performance of the detailed diagnosis and investigation. In any case, both studies show that synthesizing DOPU from OCT intensity is feasible. Therefore, synthesizing DOPU is a promising way to extract hidden features of tissues in OCT intensity.

5. Conclusion

Neural-network-based DOPU estimation algorithm was demonstrated. OCT intensity images were input to the CNN, and corresponding DOPU images were synthesized. The performance of the method was evaluated with the OCT dataset of healthy and pathological eyes. Finally, the synthesized DOPU images are similar to DOPU, and their clinical findings were also well matched. The synthesizing DOPU from OCT intensity showed the feasibility to be used in clinical diagnosis.

Funding. Core Research for Evolutional Science and Technology (JPMJCR2105); Japan Society for the Promotion of Science (JSPS) KAKENHI (18H01893, 18K09460, 21K09684, 21H01836, 22K04962), Japan Science and Technology Agency (JST) JST-Mirai program (JPMJMI18G8).

Acknowledgments. We acknowledge the help for grading to Takuya Iwasaki, Tokyo Medical University Ibaraki Medical Center, Tatsuo Yamaguchi, Topcon Corporation, for technical support and discussions, and Kensuke Oikawa for the preparation of codes.

Disclosures.

SM: Topcon (F), Tomey (P), Yokogawa Electric (F), Nikon (F), Sky Technology (F), Kao (F). KO: Topcon (F), Yokogawa Electric (F), Nikon (F), Sky Technology (F), Kao (F). MM: Santen (F). SA: Topcon (E). TM: Topcon (E). YY: Topcon (F), Tomey (P), Yokogawa Electric (F), Nikon (F), Sky Technology (F), Kao (F).

Data availability. Data underlying the results presented in this paper are not publicly available at this time but may be obtained from the authors upon reasonable request.

Appendix

A. SNR penalizing based on OCT intensity

When we want to emulate the OCT signal with more additive noise, the straightforward approach is to add a complex Gaussian random number to the complex OCT signal. However, we need to address raw complex OCT data. Hence, a method of low-SNR OCT intensity emulation using OCT intensity was implemented.

The SNR-reduced OCT intensity by adding random zero-mean Gaussian variables to complex OCT signal is described as:

$$\begin{aligned}
 |g'|^2 &= |g_{re} + n_{re} + i(g_{im} + n_{im})|^2 \\
 &= (g_{re} + n_{re})^2 + (g_{im} + n_{im})^2, \\
 &= |g|^2 + 2g_{re}n_{re} + 2g_{im}n_{im} + (n_{re}^2 + n_{im}^2)
 \end{aligned} \tag{9}$$

where g' and $g = g_{re} + ig_{im}$ are the emulated and measured complex OCT signals, n_{re} and n_{im} are emulated noises for real and imaginary parts.

If we know only OCT intensity, we have only the magnitude of g and simulated noises n_{re} and n_{im} . The point is how to calculate the 2nd and 3rd terms of Eq. 9 using OCT intensity, namely, how to assume the splitting ratio of OCT intensity into real and imaginary parts. Fortunately, we

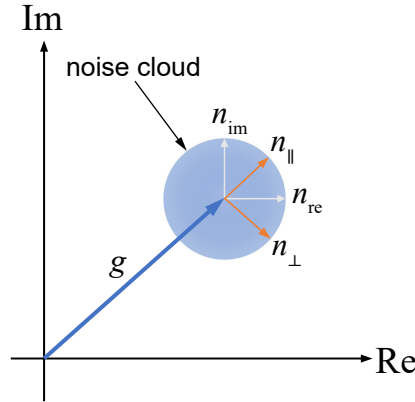


Fig. 8. The schematic relationship between measured complex OCT signal g and emulated additive noises n .

do not need to care about the ratio. If we assume complex circular Gaussian noise, i.e., n_{re} and n_{im} are independent Gaussian random variables, the selection of the coordinate of complex plane does not change the statistics of Eq. 9. Then, we can choose the simplest case, one axis along the signal phasor, g , and another perpendicular to that [Fig. 8]. By using the newly selected coordinate, we can emulate low-SNR OCT intensity with additional additive noise in complex as:

$$I' = I + 2\sqrt{I} \cdot n_{\parallel} + n_{\parallel}^2 + n_{\perp}^2, \quad (10)$$

where $I = |g|^2$ is the measured OCT intensity signal. n_{\parallel} and n_{\perp} are random Gaussian variables parallel and perpendicular to the signal phasor, g . By generating two independent random zero-mean Gaussian variables and substituting into n_{\parallel} and n_{\perp} of Eq. 10, SNR-reduced OCT intensity signal can be simulated with the only magnitude of OCT signal $\sqrt{I} = |g|$.

References

1. D. Huang, E. A. Swanson, C. P. Lin, J. S. Schuman, W. G. Stinson, W. Chang, M. R. Hee, T. Flotte, K. Gregory, C. A. Puliafito, and J. G. Fujimoto, "Optical coherence tomography," *Science* **254**, 1178–1181 (1991).
2. R. A. Costa, M. Skaf, L. A. S. Melo, D. Calucci, J. A. Cardillo, J. C. Castro, D. Huang, and M. Wojtkowski, "Retinal assessment using optical coherence tomography," *Prog. Retin. Eye Res.* **25**, 325–353 (2006).
3. E. Götzinger, M. Pircher, W. Geitzenauer, C. Ahlers, B. Baumann, S. Michels, U. Schmidt-Erfurth, and C. K. Hitzenberger, "Retinal pigment epithelium segmentation by polarization sensitive optical coherence tomography," *Opt. Express* **16**, 16410–16422 (2008).
4. B. Baumann, S. O. Baumann, T. Konegger, M. Pircher, E. Götzinger, F. Schlanitz, C. Schütze, H. Sattmann, M. Litschauer, U. Schmidt-Erfurth, and C. K. Hitzenberger, "Polarization sensitive optical coherence tomography of melanin provides intrinsic contrast based on depolarization," *Biomed. Opt. Express* **3**, 1670–1683 (2012).
5. S. Makita, Y.-J. Hong, M. Miura, and Y. Yasuno, "Degree of polarization uniformity with high noise immunity using polarization-sensitive optical coherence tomography," *Opt. Lett.* **39**, 6783–6786 (2014).
6. M. Pircher, E. Götzinger, O. Findl, S. Michels, W. Geitzenauer, C. Leydolt, U. Schmidt-Erfurth, and C. K. Hitzenberger, "Human macula investigated *in vivo* with polarization-sensitive optical coherence tomography," *Invest. Ophthalmol. Vis. Sci.* **47**, 5487–5494 (2006).
7. S. Michels, M. Pircher, W. Geitzenauer, C. Simader, E. Götzinger, O. Findl, U. Schmidt-Erfurth, and C. K. Hitzenberger, "Value of polarisation-sensitive optical coherence tomography in diseases affecting the retinal pigment epithelium," *Br. J. Ophthalmol.* **92**, 204–209 (2008).
8. B. Baumann, E. Götzinger, M. Pircher, H. Sattmann, C. Schütze, F. Schlanitz, C. Ahlers, U. Schmidt-Erfurth, and C. K. Hitzenberger, "Segmentation and quantification of retinal lesions in age-related macular degeneration using polarization-sensitive optical coherence tomography," *J. Biomed. Opt.* **15**, 061704 (2010).
9. C. Ahlers, E. Götzinger, M. Pircher, I. Golbaz, F. Prager, C. Schütze, B. Baumann, C. K. Hitzenberger, and U. Schmidt-Erfurth, "Imaging of the Retinal Pigment Epithelium in Age-Related Macular Degeneration Using Polarization-Sensitive Optical Coherence Tomography," *Invest. Ophthalmol. Vis. Sci.* **51**, 2149–2157 (2010).

10. F. G. Schlanitz, B. Baumann, T. Spalek, C. Schütze, C. Ahlers, M. Pircher, E. Götzinger, C. K. Hitzenberger, and U. Schmidt-Erfurth, "Performance of Automated Drusen Detection by Polarization-Sensitive Optical Coherence Tomography," *Invest. Ophthalmol. Vis. Sci.* **52**, 4571–4579 (2011).
11. J. Lammer, M. Bolz, B. Baumann, M. Pircher, E. Götzinger, G. Mylonas, C. K. Hitzenberger, and U. Schmidt-Erfurth, "Imaging Retinal Pigment Epithelial Proliferation Secondary to PASCAL Photocoagulation *In Vivo* by Polarization-sensitive Optical Coherence Tomography," *Am. J. Ophthalmol.* **155**, 1058–1067 (2013).
12. C. Schütze, M. Bolz, R. Sayegh, B. Baumann, M. Pircher, E. Götzinger, C. K. Hitzenberger, and U. Schmidt-Erfurth, "Lesion Size Detection in Geographic Atrophy by Polarization-Sensitive Optical Coherence Tomography and Correlation to Conventional Imaging Techniques," *Invest. Ophthalmol. Vis. Sci.* **54**, 739–745 (2013).
13. M. Ritter, S. Zotter, W. M. Schmidt, R. E. Bittner, G. G. Deak, M. Pircher, S. Sacu, C. K. Hitzenberger, and U. M. Schmidt-Erfurth, "Characterization of Stargardt Disease Using Polarization-Sensitive Optical Coherence Tomography and Fundus Autofluorescence Imaging," *Invest. Ophthalmol. Vis. Sci.* **54**, 6416–6425 (2013).
14. R. G. Sayegh, S. Zotter, P. K. Roberts, M. M. Kandula, S. Sacu, D. P. Kreil, B. Baumann, M. Pircher, C. K. Hitzenberger, and U. Schmidt-Erfurth, "Polarization-sensitive optical coherence tomography and conventional retinal imaging strategies in assessing foveal integrity in geographic atrophy," *Invest. Ophthalmol. Vis. Sci.* **56**, 5246–5255 (2015).
15. F. G. Schlanitz, S. Sacu, B. Baumann, M. Bolz, M. Platzer, M. Pircher, C. K. Hitzenberger, and U. Schmidt-Erfurth, "Identification of Drusen Characteristics in Age-Related Macular Degeneration by Polarization-Sensitive Optical Coherence Tomography," *Am. J. Ophthalmol.* **160**, 335–344.e1 (2015).
16. P. Roberts, B. Baumann, J. Lammer, B. Gerendas, J. Kroisamer, W. Bühl, M. Pircher, C. K. Hitzenberger, U. Schmidt-Erfurth, and S. Sacu, "Retinal pigment epithelial features in central serous chorioretinopathy identified by polarization-sensitive optical coherence tomography," *Invest. Ophthalmol. Vis. Sci.* **57**, 1595–1603 (2016).
17. M. Miura, S. Makita, S. Sugiyama, Y.-J. Hong, Y. Yasuno, A. E. Elsner, S. Tamiya, R. Tsukahara, T. Iwasaki, and H. Goto, "Evaluation of intraretinal migration of retinal pigment epithelial cells in age-related macular degeneration using polarimetric imaging," *Sci. Rep.* **7**, 3150 (2017).
18. M. Miura, S. Makita, S. Azuma, Y. Yasuno, S. Ueda, S. Sugiyama, T. Mino, T. Yamaguchi, H. S. Sandhu, H. J. Kaplan, T. Iwasaki, and H. Goto, "Evaluation of focal damage in the retinal pigment epithelium layer in serous retinal pigment epithelium detachment," *Sci. Rep.* **9**, 3278 (2019).
19. M. Miura, S. Makita, S. Azuma, Y. Yasuno, S. Sugiyama, T. Mino, T. Yamaguchi, T. Agawa, T. Iwasaki, Y. Usui, N. A. Rao, and H. Goto, "Evaluation of Retinal Pigment Epithelium Layer Change in Vogt-Koyanagi-Harada Disease With Multicontrast Optical Coherence Tomography," *Invest. Ophthalmol. Vis. Sci.* **60**, 3352–3362 (2019).
20. M. Miura, S. Makita, Y. Yasuno, T. Iwasaki, S. Azuma, T. Mino, and T. Yamaguchi, "Evaluation of retinal pigment epithelium changes in serous pigment epithelial detachment in age-related macular degeneration," *Sci. Rep.* **11**, 2764 (2021).
21. D. Bicout, C. Brosseau, A. S. Martinez, and J. M. Schmitt, "Depolarization of multiply scattered waves by spherical diffusers: Influence of the size parameter," *Phys. Rev. E* **49**, 1767–1770 (1994).
22. S. P. Morgan, M. P. Khong, and M. G. Somekh, "Effects of polarization state and scatterer concentration on optical imaging through scattering media," *Appl. Opt.* **36**, 1560–1565 (1997).
23. M. I. Mischenko and J. W. Hovenier, "Depolarization of light backscattered by randomly oriented nonspherical particles," *Opt. Lett.* **20**, 1356–1358 (1995).
24. B. Karamata, M. Laubscher, M. Leutenegger, S. Bourquin, T. Lasser, and P. Lambelet, "Multiple scattering in optical coherence tomography. I. Investigation and modeling," *J. Opt. Soc. Am. A* **22**, 1369–1379 (2005).
25. T. R. Hillman, A. Curatolo, B. F. Kennedy, and D. D. Sampson, "Detection of multiple scattering in optical coherence tomography by speckle correlation of angle-dependent B-scans," *Opt. Lett.* **35**, 1998–2000 (2010).
26. M. T. McCann, K. H. Jin, and M. Unser, "Convolutional Neural Networks for Inverse Problems in Imaging: A Review," *IEEE Signal Process. Mag.* **34**, 85–95 (2017).
27. B. Rahmani, D. Loterie, G. Konstantinou, D. Psaltis, and C. Moser, "Multimode optical fiber transmission with a deep learning network," *Light Sci. Appl.* **7**, 69 (2018).
28. T. Seesan, I. A. El-Sadek, P. Mukherjee, L. Zhu, K. Oikawa, A. Miyazawa, L. T.-W. Shen, S. Matsusaka, P. Buranasiri, S. Makita, and Y. Yasuno, "Deep convolutional neural network-based scatterer density and resolution estimators in optical coherence tomography," *Biomed. Opt. Express* **13**, 168–183 (2022).
29. O. Ronneberger, P. Fischer, and T. Brox, "U-Net: Convolutional Networks for Biomedical Image Segmentation," in *Medical Image Computing and Computer-Assisted Intervention – MICCAI 2015*, N. Navab, J. Hornegger, W. M. Wells, and A. F. Frangi, eds. (Springer International Publishing, Cham, 2015), Lecture Notes in Computer Science, pp. 234–241.
30. J. L. Ba, J. R. Kiros, and G. E. Hinton, "Layer Normalization," arXiv (2016).
31. A. L. Maas, A. Y. Hannun, and A. Y. Ng, "Rectifier nonlinearities improve neural network acoustic models," in *In ICML Workshop on Deep Learning for Audio, Speech and Language Processing*, (2013).
32. S. Makita, T. Mino, T. Yamaguchi, M. Miura, S. Azuma, and Y. Yasuno, "Clinical prototype of pigment and flow imaging optical coherence tomography for posterior eye investigation," *Biomed. Opt. Express* **9**, 4372–4389 (2018).
33. M. J. Ju, Y.-J. Hong, S. Makita, Y. Lim, K. Kurokawa, L. Duan, M. Miura, S. Tang, and Y. Yasuno, "Advanced multi-contrast Jones matrix optical coherence tomography for Doppler and polarization sensitive imaging," *Opt. Express* **21**, 19412–19436 (2013).

34. D. P. Kingma and J. Ba, "Adam: A Method for Stochastic Optimization," arXiv:1412.6980v9 (2017).
35. G. A. D. O'Keefe and N. A. Rao, "Vogt-Koyanagi-Harada disease," *Surv. Ophthalmol.* **62**, 1–25 (2017).
36. M. Miura, S. Makita, Y. Yasuno, R. Tsukahara, Y. Usui, N. A. Rao, Y. Ikuno, S. Uematsu, T. Agawa, T. Iwasaki, and H. Goto, "Polarization-sensitive optical coherence tomographic documentation of choroidal melanin loss in chronic Vogt–Koyanagi–Harada disease," *Invest. Ophthalmol. Vis. Sci.* **58**, 4467–4476 (2017).
37. M. Miura, S. Makita, Y. Yasuno, S. Azuma, T. Mino, T. Yamaguchi, T. Iwasaki, R. Nemoto, H. Shimizu, and H. Goto, "Objective evaluation of choroidal melanin loss in patients with Vogt–Koyanagi–Harada disease using polarization-sensitive optical coherence tomography," *Sci. Rep.* **12**, 3526 (2022).
38. D. Ulyanov, A. Vedaldi, and V. Lempitsky, "Instance Normalization: The Missing Ingredient for Fast Stylization," arXiv:1607.08022v3 (2017).
39. Y. Sun, J. Wang, J. Shi, and S. A. Boppart, "Synthetic polarization-sensitive optical coherence tomography by deep learning," *npj Digit. Med.* **4**, 1–7 (2021).
40. P. Isola, J.-Y. Zhu, T. Zhou, and A. A. Efros, "Image-to-Image Translation with Conditional Adversarial Networks," in *2017 IEEE Conference on Computer Vision and Pattern Recognition (CVPR)*, (IEEE, Honolulu, HI, 2017), pp. 5967–5976.
41. X. Wang and L. V. Wang, "Propagation of polarized light in birefringent turbid media: A Monte Carlo study," *J. Biomed. Opt.* **7**, 279 (2002).
42. S. L. Jacques, J. R. Roman, and K. Lee, "Imaging superficial tissues with polarized light," *Lasers Surg. Med.* **26**, 119–129 (2000).